Size dependent thermal conductivity of single-walled carbon nanotubes

Ajing Cao and Jianmin Qu

Citation: J. Appl. Phys. **112**, 013503 (2012); doi: 10.1063/1.4730908
View online: http://dx.doi.org/10.1063/1.4730908
View Table of Contents: http://jap.aip.org/resource/1/JAPIAU/v112/i1
Published by the American Institute of Physics.

Size dependent thermal conductivity of single-walled carbon nanotubes

Ajing Cao[1,a)] and Jianmin Qu[1,2,b)]
[1]*Department of Civil and Environmental Engineering, Northwestern University, Evanston, Illinois 60208, USA*
[2]*Department of Mechanical Engineering, Northwestern University, Evanston, Illinois 60208, USA*

(Received 29 February 2012; accepted 26 May 2012; published online 3 July 2012)

In this paper, we report a non-equilibrium molecular dynamics study on the size-dependent thermal conductivity in single-walled carbon nanotubes with lengths up to micrometers at room temperature. It is found that the size-dependent thermal conductivity of single-walled carbon nanotubes can be described by $\kappa(L,d) \approx \kappa_g(L)(1 - e^{-0.185d/a_0})$, where L is the tube length, d is the diameter, $a_0 = 2.46$ Å is the graphene lattice constant, and $\kappa_g(L) \propto L^{\alpha}$ is the thermal conductivity of a graphene of length L. In the above, $\alpha = 1$ for $L < l_0$, and $\alpha \sim 0.21$ for $L > l_0$, independent of the tube chirality (zigzag or armchair), where $l_0 \approx 200$ nm and 300 nm are the effective phonon mean free path for zigzag and armchair tubes, respectively. Physical interpretations of such geometry dependence are provided in the paper by analyzing the spectral energy density, the dispersion relationship, the phonon density of state, and the power spectrum of phonons. © *2012 American Institute of Physics*. [http://dx.doi.org/10.1063/1.4730908]

I. INTRODUCTION

Because of its unique thermal, electrical, and mechanical properties, carbon nanotube (CNT) is becoming a promising candidate for future nano-electro-mechanical system (NEMS).[1–3] In particular, CNTs have been studied extensively as thermal interface materials to dissipate heat in NEMS. Recently, graphene, a one-layer crystal arranged in a two-dimensional honeycomb lattice of carbon bonds, has attracted a great deal of attention from the physics and engineering communities owing to its exceptional properties such as thermal conductivity.[2–8] However, existing studies have shown inconsistent results on the thermal conductivity of CNTs and graphene. For example, the reported room temperature thermal conductivity of single-walled CNT (SWCNT) ranges widely from 30 to 400 000 W/mK.[1,9–28] In particular, the range of values predicted by either theoretical or numerical models is extremely large. For example, Che *et al.*[28] utilizing molecular dynamics (MD) simulations found that the transition length to fully diffusive regime is 40 nm, and the diffusive thermal conductivity is about 3000 W/m K at room temperature. Yao *et al.*[11] calculated thermal conductivity of SWCNTs to be 400 000 W/mK for (10, 10) with length of 100 nm using the Green-Kubo method. Maruyama[12] showed that the thermal conductivity is around 400 W/m K for a 400 nm long tube and increases steadily with length with an exponent of 0.15. Mingo and Broido[29] solved the linearized Boltzmann–Peierls phonon transport equation by accounting the three-phonon scattering processes to higher order and showed that the room temperature thermal conductivity of a 100 nm-long (10, 0) SWNT is 100 W/mK and can be as high as 9500 W/mK in the fully diffusive regime. More recently, Lindsay *et al.*[27] showed that, by using the correct phonon selection rules within the phonon transport framework, the thermal conductivity of SWCNTs does not converge until its length reaches millimeter range and the length-converged value is about 6000 W/mK at room temperature. More recent experimental measurements on a 2.6 μm long SWCNT show a peak thermal conductivity value of about 3400 W/mK at 300 K, and the value decreases to about 1200 W/mK at 800 K.[23] Clearly, the thermal conductivity of SWCNT is a strong function of the CNT length.

Another factor that has not been called to attention is the diameter dependence. The diameters of typical SWCNTs by chemical vapor deposition (CVD) methods are typically around 5–20 nm,[12,16] while the most commonly studied SWCNTs in MD simulations are smaller than 2 nm in diameter. Therefore, it is imperative to know the dependence of the thermal conductivity of SWCNTs on its diameter. Unfortunately, there has been very little work done in this area until recently, and the results are inconsistent. Thomas *et al.*[16] reported that the thermal conductivity of SWCNTs decreases monotonically with increasing tube diameter with the thermal conductivity of graphene as the lower limit, while Lindsay *et al.*[30] reported exactly the opposite trend, i.e., the thermal conductivity increases with tube diameter with the thermal conductivity of graphene as the upper limit.

In an effort to clarify the confusion, and to understand the discrepancy in the existing literature, we investigate the size-dependent thermal conductivity of SWCNT in this work. Specifically, we use a classical non-equilibrium MD simulation method[12,13] to calculate the thermal conductivity of SWCNTs with radii ranging from (5, 5) to (40, 40) for armchair SWCNTs and (5, 0) to (60, 0) for zigzag SWCNTs, and lengths ranging from 5 nm to 2.5 μm. The optimized Tersoff potential[31] is used in the MD simulations. A schematic of the simulation models used in the present work is shown in Figure 1. The same method was used in our recent work on Kapitza conductance of symmetric tilt grain boundaries in graphene.[32]

We note that classical MD simulations such as the one used in this work neglect the explicit description of

[a)]Present address: MST-8, Los Alamos National Laboratory, Los Alamos, New Mexico, 87544, USA. Email: acao@lanl.gov.
[b)]Email: j-qu@northwestern.edu.

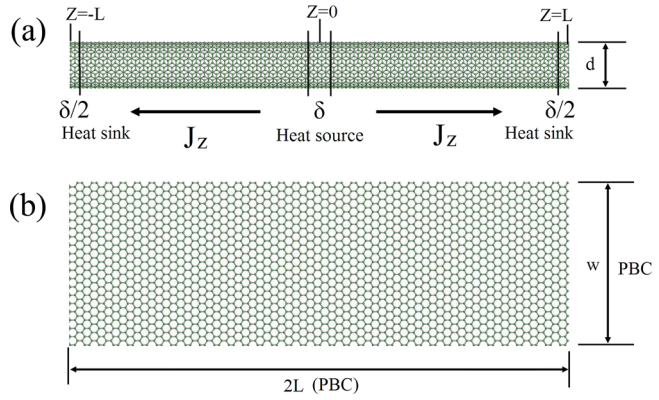

FIG. 1. Schematics of the simulation cells for the SWCNT (a) and graphene (b). The half-length L of the simulation cell ranges from 20 nm to 2500 nm. The heat source is placed over a region of length δ centered at $Z=0$, and a heat sink is placed over a region of length $\delta/2$ at each end of the tube/graphene ribbon. Periodic boundary conditions are prescribed in all three orthogonal directions of the simulation cell.

electrons. However, it has been shown that the electron mediated thermal transport in SWNTs is negligibly small in comparison with the phonon mediated thermal transport at room temperature.[33,34] Therefore, classical MD can be used to simulate the thermal transport in SWCNTs at room temperatures.

Thermal transport in SWCNTs generally can be categorized into three different regimes.[35] In tubes with lengths less than the effective phonon mean free path (MFP) l_0, the transport is ballistic. When the tube is longer than the diffusive transition length l_∞, the transport becomes fully diffusive and the thermal conductivity becomes length-independent. In between l_0 and l_∞, it is a gradual transition from ballistic to diffusive transport. Such a transition is the result of two phonon scattering processes, namely, phonon-boundary scattering and phonon-phonon scattering. In very short SWCNTs ($\ll l_0$), the thermal resistance due to boundary scattering dominates. In comparison, thermal resistance due to phonon-phonon scattering is negligible, and the thermal transport is predominately ballistic. As the SWCNT length increases beyond l_0, the effect of boundary scattering decreases and the effect of phonon-phonon scattering gradually becomes the major source of thermal resistance. As the SWCNT length further increases beyond l_∞, boundary scattering diminishes significantly so that thermal resistance is primarily due to phonon-phonon scattering. Thus, thermal transport becomes fully diffusive and thermal conductivity becomes almost independent of the tube length. The regime between the predominately ballistic to fully diffusive is called the ballistic-diffusive transition regime because both phonon-boundary scattering and phonon-phonon scattering co-exist. Our main focus in this paper is the size (length and diameter) dependence of thermal conductivity in this ballistic-diffusive transition regime, with special attention to the potential and simulation technique being chosen.

We believe that this is the first report on full MD simulations of experimentally employed micrometer-long SWCNTs. All previous work in this area had been for much shorter SWCNTs. Since the ballistic length is about 200 nm, the transition from ballistic to diffusive regimes is between hundreds of nanometers to micrometers, which is the focus of the present paper. Although it is well known that the thermal conductivity of SWCNTs scales up with their length in the ballistic regime, the length-dependence of thermal conductivity of SWCNT in the ballistic-diffusive transition regimes is not well established and cannot be extrapolated from the ballistic regime. This makes it necessary to directly compute the thermal conductivity of SWCNTs whose lengths are in the ballistic-diffusive transition regime.

II. METHOD

Analogous to many experimental setups for measuring SWCNT thermal conductivity,[17,23] the non-equilibrium MD method imposes a temperature gradient by applying a heat flux along the SWCNT axial direction. Thermal conductivity of SWCNT can then be obtained from the heat flux and the temperature gradient along the tube using the well-known Fourier's law,

$$\kappa = -\frac{J_z}{\partial T/\partial z}, \tag{1}$$

where J_z is the heat flux, and $\partial T/\partial z$ is the spatial temperature gradient. In our calculations, the heat source is placed at the middle of the tube and a heat sink is attached to each end of the tube. Period boundary conditions (PBCs) are used along the tube axial direction, see Figure 1(a). The energy transport algorithm proposed by Jund and Jullien[36] is employed. In this manner, once a steady state (i.e., the temperature profile along the tube does not change with time) is reached, a constant temperature gradient from the center to each end is established. After reaching the steady state condition, averages over 100 ps time are used to perform ensemble sampling. Such statistically averaged temperature profile is then used to compute the temperature gradient using a standard linear regression method. Standard deviation associated with the linear regression of the temperature profile is reported in our results by error bars.

In using Eq. (1), one needs to know the SWCNT cross-section area in order to compute the heat flux J_z. We follow the standard practice of treating the SWCNT as a hollow tube of diameter d, and a wall thickness of $h = 3.4$ Å. This gives the cross-section area of πdh. For graphene, the cross-section area is wh, where w is the width of the graphene sheet. A schematic of the simulation models used in the present work is shown in Figure 1.

Prior to applying the heat flux, a NPT ($P=0$, $T=300$ K) ensemble run followed by a NVE run is performed to ensure that the SWCNT is thermo-mechanically equilibrated. The system temperature is found to be fairly constant around 300 K with very little fluctuation for the remaining data collection run. The velocity Verlet integration method with a time step of 0.5 fs is used. The LAMMPS software package[37] is used for carrying out all MD simulations. The simulations for the case of $2L = 4800$ nm (10, 10) SWCNT consisting of 787 200 atoms took about 5 days on a computer cluster with

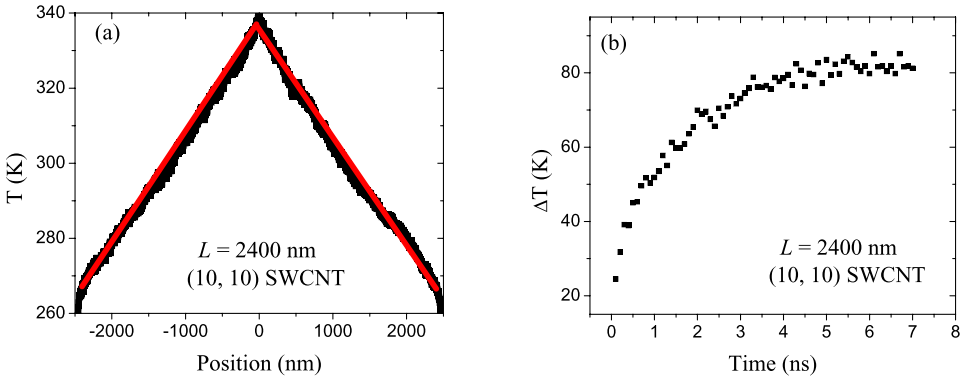

FIG. 2. (a) The temperature profile for the 2400 nm-long (10, 10) SWCNT, showing clearly a linear temperature distribution. (b) The temperature difference between the heat source and heat sink evolves with time, showing that the time to reach steady state is ~6 ns.

120 cpu cores (Intel X5650, 64-bit, 2.26 GHz, 48 GB memory).

Similar MD simulation methodologies are also used for calculating the thermal conductivity of graphene. Graphene ribbons of width $w = 5.2$ nm and length L are used in the simulations. Periodic boundary conditions are used in all four sides of the ribbon. This effectively simulates a graphene sheet of infinite width instead of a ribbon with free edges. We have found that doubling the ribbon width introduces no significant difference in the results, indicating that 5.2 nm is wide enough so that the results are independent of the width of the simulation cell. In addition, varying the size of heat source and sink from 2 nm to 10 nm does not change the results.

Here, we stress that the optimized Tersoff potential[31] is used in our MD simulations for a number of reasons. In comparison to the original Tersoff[38] and the Brenner[39] potentials, the optimized Tersoff potential provides a more accurate description of the thermal properties in SWCNTs because (1) the optimized Tersoff potential predicts better fits to some structural data and most importantly the in-plane phonon-dispersion data for graphite;[40,41] (2) group velocities of the acoustic modes predicted by the optimized Tersoff potential are much closer to the reported experimental values, although the group velocities of TA over a half of the Brillouin zone are a little overestimated;[40,41] (3) the calculated thermal conductivity based on the optimized Tersoff potential agrees well with the results from phonon Boltzmann transport equation approach;[30] and (4) more importantly, the thermal conductivity calculated using the optimized Tersoff potential as reported here is much closer to the experimental data.[23]

III. RESULTS AND DISCUSSION

A representative temperature profile for a 2400 nm-long (10, 10) SWCNT is shown in Figure 2(a). To ensure long enough simulation time to reach steady state, we have monitored the temperature difference ΔT between the heat source and the heat sink as a function of simulation time. From Figure 2(b), it is clear that ΔT approaches a constant value after ~6 ns, meaning that the time for reaching steady state for the 2400 nm-long (10, 10) SWCNT is ~6 ns. A summary of the simulation details we used is listed in Table I.

Shown in Figure 3 are our results for the thermal conductivity of both armchair and zigzag SWCNTs along with that of graphene at $T = 300$ K. It is seen that both the zigzag and armchair SWCNTs show similar trend, i.e., the thermal conductivity increases with increasing tube length. Careful analysis of the data shows that the thermal conductivity depends on the tube length through $\kappa(L) \propto L^{\alpha}$, where $\alpha \sim 1$ for $L < l_0$ and $\alpha \sim 0.21$ for $L > l_0$ in the range of tube diameters considered here, and $l_0 = 200$ nm for zigzag and for $l_0 = 300$ nm for armchair tubes. One may thus conclude from these results that the MFP is $l_0 \approx 200$ nm and 300 nm for zigzag and armchair tubes, regardless of the diameter. This is consistent with the experimental results.[23] For shorter tubes ($L < l_0$), the transport is predominantly ballistic, e.g., lattice anharmonicity, in comparison with the boundary scattering, has negligible effect on heat conduction[29] and the thermal conductivity scales with the tube length ($\alpha \sim 1$). For longer tubes ($L > l_0$), the transport is both ballistic and diffusive and the thermal conductivity is a power law function of the tube length with an exponent less than unity. As the tube length increases, thermal transport becomes more and more diffusive. Although it is expected that beyond certainly tube length l_{∞}, thermal transport would become fully diffusive and the thermal conductivity should become independent of the tube length, we have not been able to find such transition length at which the transport is fully diffusive, because our computational resources limited us to tube length no more than several micrometers. A recent study[27] using the phonon Boltzmann transport equation approach, however, seems to have shown that thermal transport in SWCNT does not become fully diffusive until the tube length is in the millimeter range.

To further investigate the size dependence of the thermal conductivity, we examine the spectral energy density

TABLE I. The heat flux and total MD simulation time for simulating various lengths with the optimized Tersoff potential used in the present study.

Length (nm)	100	400	600	1000	1200	1800	2400
Heat flux (eV/(ps Å^2))	0.000688	0.001377	0.001377	0.001377	0.001377	0.002754	0.002754
Simulation time (ns)	0.1	0.4	1.0	1.6	2	4	7

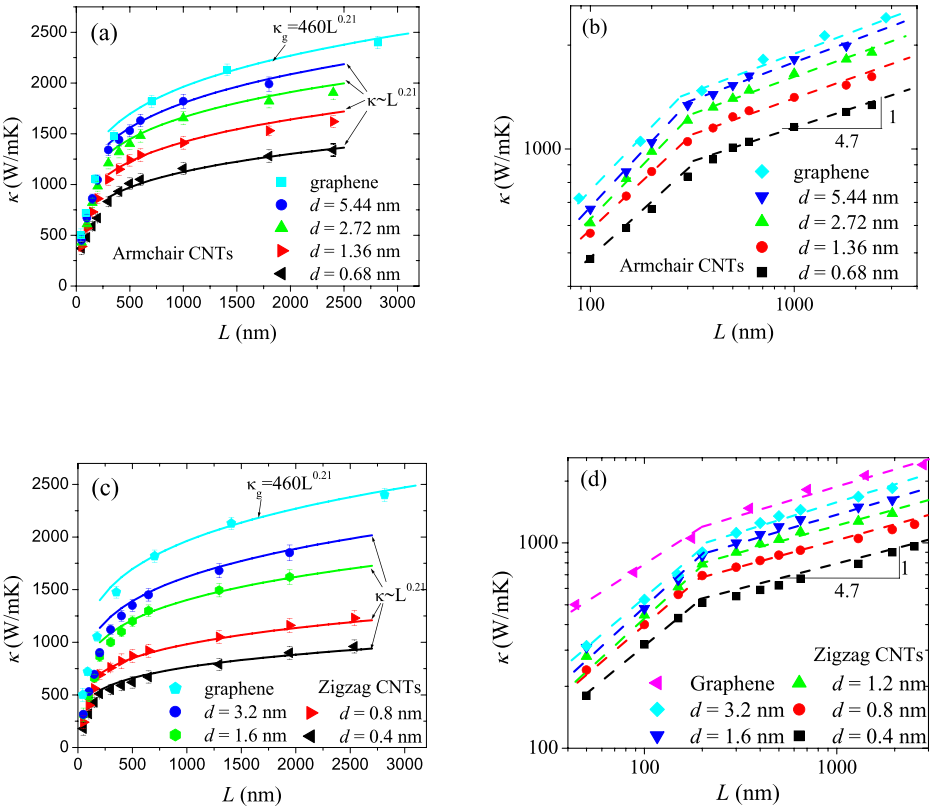

FIG. 3. Thermal conductivity κ as a function of tube length for (a) armchair and (c) zigzag tubes compared with that of graphene. (b) and (d) are the log-log plots of (a) and (c), respectively, showing the transition from linear to a power-law function of L at about 300 nm, and 200 nm for armchair and zigzag SWCNTs, respectively. The error bars were calculated based on the uncertainty involved in the linear regression of the temperature gradient along the tube.

(SED), which gives the average kinetic energy per atom as a function of wave vector and frequency. The SED can be described by the following time-space 2-D Fourier transform in the cylindrical coordinate system (r, φ, z)[24]

$$E(\omega,\mathbf{k}) = E_z(\omega,\mathbf{k}) + E_r(\omega,\mathbf{k}) + E_\varphi(\omega,\mathbf{k}), \tag{2}$$

where

$$E_\alpha(\omega,\mathbf{k}) = \frac{1}{3\tau_0 Nn}\sum_{q=1}^{n} m_q \left| \sum_{p=1}^{N} \int_0^{\tau_0} v_\alpha(p,q,t)\exp(i\mathbf{k}\cdot\mathbf{r}_{qp} - i\omega t)dt \right|^2, \quad \alpha = z,r,\varphi \tag{3}$$

can be regarded as the SED of polarization $\alpha(=z, r, \varphi)$. In the above, ω is the frequency, $\mathbf{k}$ is the wave vector, N is the number of unit cells in the system, n is the number of atoms in each unit cell, $v_\alpha(p, q, t)$ is the α component of the atom velocity, $\mathbf{r}_{qp}$ is the atom coordinate vector, m_q is the mass, all for the qth atom in the pth unit cell, and τ_0 is the total integration time. The atom velocity components (v_z, v_φ, v_r) correspond to, respectively, the longitudinal, twist, and radial breathing polarization of the vibration modes. Once the atom velocity $v_\alpha(p, m, t)$ is computed using the MD simulations under the *NVE* ensemble, the SED can be obtained from carrying out the integration and summations in Eq. (3). We note that the full temperature-dependent anharmonicity of atomic interactions is accounted for in computing the SED.

The results for $E(\omega, k_z)$ based our MD simulations using the optimized Tersoff potential are shown in Figure 4 for the (5, 5) and (40, 40) tubes. Note that because the SED defined here in Eq. (2) is already on a per atom basis, the comparison for tubes with different diameters is therefore meaningful. Although the overall features of Figure 4 agree well with the existing theoretical predictions,[42] our results shown in Figure 4 are much closer to the experimental data.[40,41] It is seen that the longitudinal optical (LO) and transverse optical (TO) modes accurately reproduce the well-known G-band in the Raman spectra of graphene at 1580 cm^{-1} (corresponding to ~50 THz)[41,43] and the corresponding modes in SWCNTs with numerical calculations.[33,34]

The next parameter of interest is the total phonon density of states (DOS) which can be calculated from the spectra energy density by summing all the phonon modes with their corresponding amplitude at a given frequency,[12] i.e.,

$$g(\omega) = \sum_\alpha g_\alpha(\omega), \quad g_\alpha(\omega) = \int_0^1 E_\alpha(\omega, k_z)dk_z, \quad \alpha = z,r,\varphi, \tag{4}$$

where $g_z(\omega)$, $g_\varphi(\omega)$, $g_r(\omega)$ are the DOS for the longitudinal, twist, and radial breathing modes, respectively. Figure 5 shows the total DOS for the (10, 10) SWCNTs of different lengths. We note that the characteristic frequencies shown in agree well with existing results. For examples, our predicted peak at 50 THz has been well documented.[41,43]

It is clearly seen from Figure 5 that longer tubes have higher DOS in entire frequency spectrum, indicating that both low and high frequency modes are enhanced in longer SWCNTs. However, these higher frequency modes are short ranged and localized. They do not contribute significantly to the thermal conductivity along the axial direction. Major

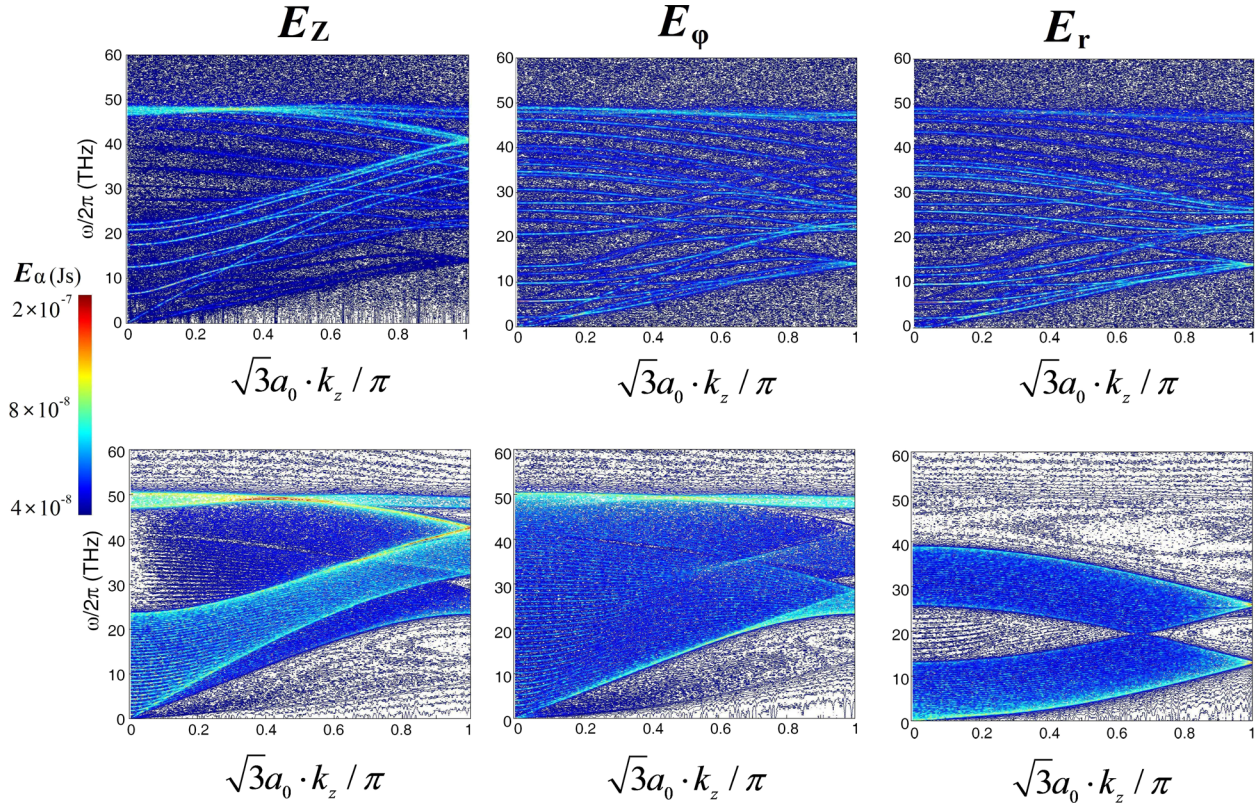

FIG. 4. The spectral energy density (SED). The top three figures are for the (5, 5) tube, and the bottom three are for the (40, 40) tube. Both tubes are 100 nm-long SWCNT at $T = 300$ K. The color indicates the magnitude of the SED at a given point (k_z, ω). From the left to the right are the longitudinal modes E_z, twist modes E_φ, and radial breathing modes E_r, respectively.

contributions to the higher conductivity in longer tubes mainly come from the enhanced low frequency modes, which are long ranged and delocalized. Our simulation results also show that $g_z(\omega)$, $g_\varphi(\omega)$, $g_r(\omega)$ have very similar variation with increasing tube length.

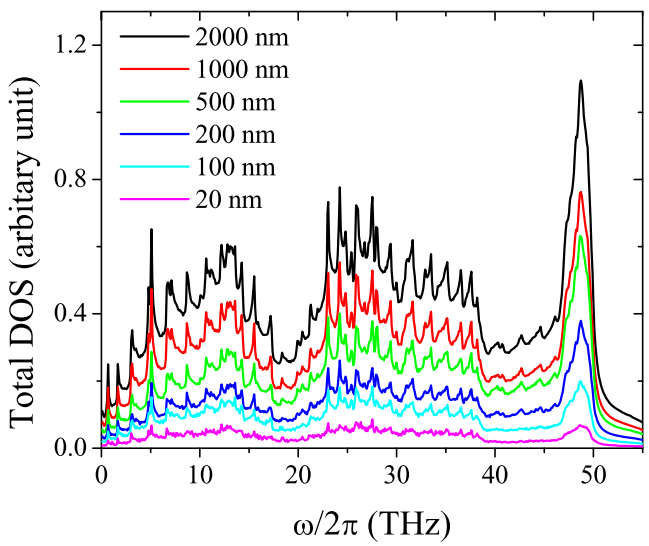

FIG. 5. The total density of state (DOS) obtained from the spectral energy density (SED) for the (10, 10) SWCNT at various tube lengths, showing the increase of total DOS with increasing SWCNT length. Note that the DOS is already normalized on a per atom basis, so that the DOS for different tube length are comparable.

Before proceeding to the diameter dependence, it is worth noting that our numerical results also show that the thermal conductivity of graphene has the same length dependence as that of the SWCNT, i.e., $\kappa_g(L) \propto L^\alpha$, where the values of α are the same as in the SWCNTs in the same heat conducting directions (see Figure 3).

Now, let us now consider the dependence of thermal conductivity of SWCNTs on tube diameter. As seen from Figure 6 that the thermal conductivity increases almost exponentially with increasing tube diameter $\kappa(L, d) \approx \kappa_g(L)(1 - e^{-0.185d/a_0})$ for both types of SWCNTs of length L, where d is the SWCNT diameter and $a_0 = 2.46$ Å is the graphene lattice constant. To gain insights on such diameter dependence, we turn our attention to the phonon dispersion curves, from which group velocity of each phonon mode can be derived. The dispersion curves can be obtained by connecting the "peaks" of the spectrum energy density plot at different wavenumbers. Figures 7(a)–7(c) show the longitudinal acoustic (LA), twist acoustic (TA), and radial breathing acoustic (ZA) phonon modes, respectively, in the armchair SWCNTs of different diameters along with that of graphene. It is seen that the dispersion curves for the LA and TA modes are very similar among SWCNTs with different diameters. The ZA mode, on the other hand, changes significantly as the tube diameter increases. Also, the difference between the dispersion curves of SWCNT and graphene is mainly in the ZA modes due to the curvature of SWCNT surfaces, i.e., as the tube diameter increases, the dispersion curve of the ZA mode approaches that of graphene, which is a quadratic

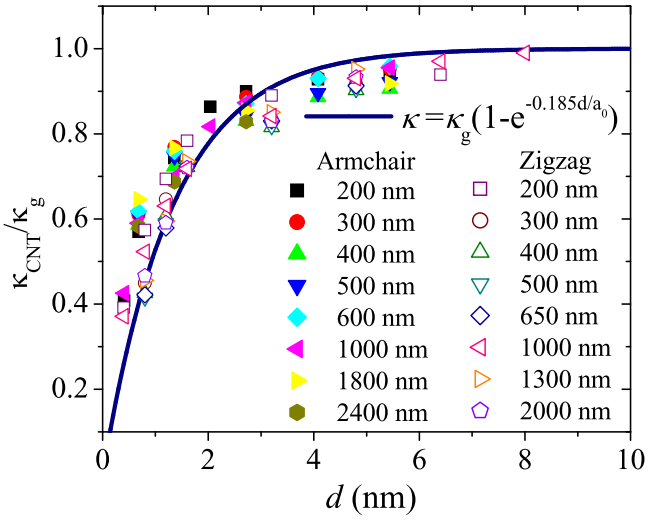

FIG. 6. Diameter dependence of the thermal conductivity for various SWCNTs at $T = 300$ K, showing all the data following a universal fitting curve. All values are normalized with the value of graphene (κ_g) of the same length.

function of k_z. Intuitively, SWCNT can be viewed as a rolled-up graphene sheet. In this regards, when a graphene sheet is ''rolled'' into a SWCNT, the 2-D dispersion band structure folds into a large number of 1-D subbands. In a (5, 5) tube, for instance, the six phonon bands (four acoustic, two degenerated transverse modes[44] and three optical) of graphene become 36 separate 1-D discernible subbands, see, e.g., Figure 4. As a result of such folding, a number of sharp peaks appear on the SWCNT phonon DOS due to 1-D van Hove singularities,[45,46] which are absent in graphene and graphite. Despite the presence of these singularities, the overall shape of phonon DOS is similar for all SWCNTs. The phonon modes calculated here based on the SED are in good agreement with what has been studied in Saito *et al.*[9,44] and Sanchez-Portal *et al.*[47] We also notice that the number of optical branches increases with the SWCNT diameter and the spacing between these branches is reduced.

At this point, it is worthwhile to discuss how the phonon modes in a SWCNT correspond to the phonon modes in a graphene sheet. In a SWCNT, the longitudinal, twist, and radial breathing modes are commonly used to describe the vibrational motion of the tube, while in a graphene sheet, in-plane longitudinal, in-plane transverse, and out-of-plane (flexural) modes are typically used. Because the SWCNT is a rolled-up graphene strip, the radial breathing and the twist modes of a SWCNT correspond to the flexural, and the in-plane transverse modes in the corresponding graphene sheet, respectively, while the longitudinal mode in the SWCNT corresponds to the in-plane longitudinal modes in the graphene. This is how the phonon modes of graphene are grouped together with those of SWCNT in Figure 7.

To further understand the diameter dependence, the DOS for the longitudinal, twist, and radial breathing modes including both acoustic and optical modes are plotted in Figures 8(a)–8(c), respectively, for tubes with different diameters. It is seen that, in comparison with the other two modes, the DOS for the radial breathing mode is rather sensitive to tube diameter, corroborating the observation in the previous paragraph that the radial breathing modes are responsible for

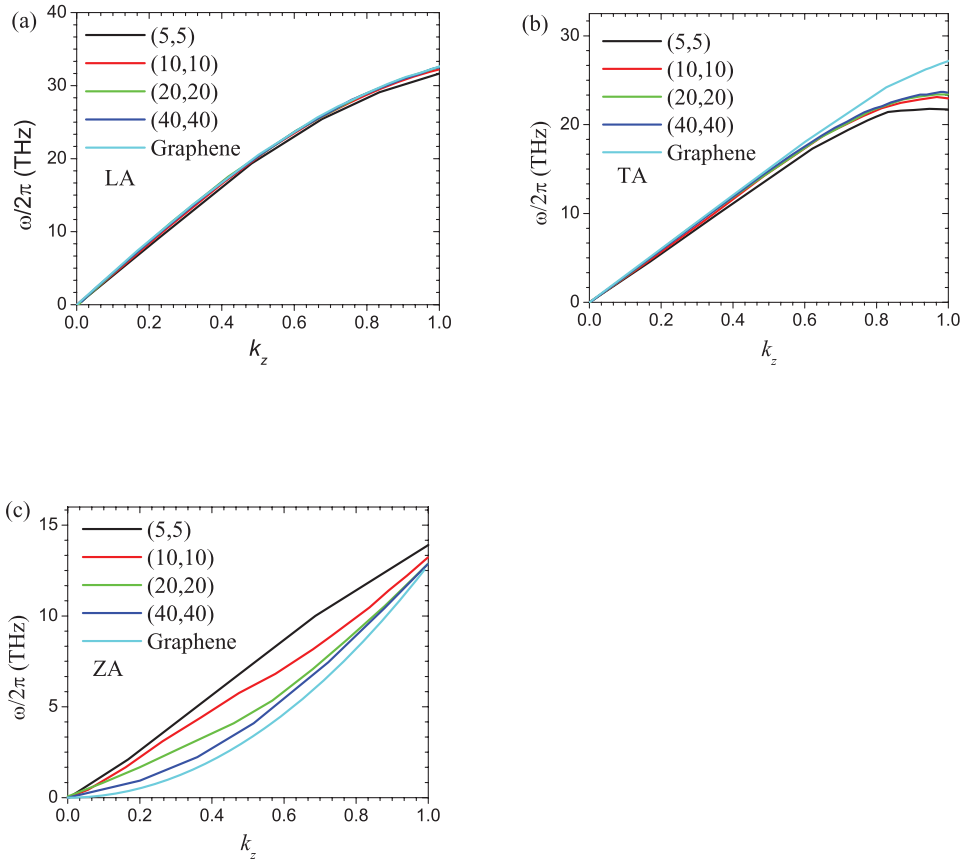

FIG. 7. Dispersion curves of the three acoustic modes in graphene and SWCNTs of different diameters. Noticeable difference is observed for radial breathing acoustic mode (ZA) among tubes with different diameters, while the other two acoustic modes (LA and TA) show very little variation.

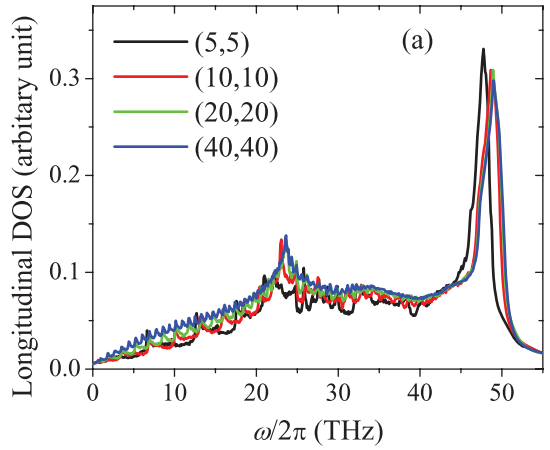

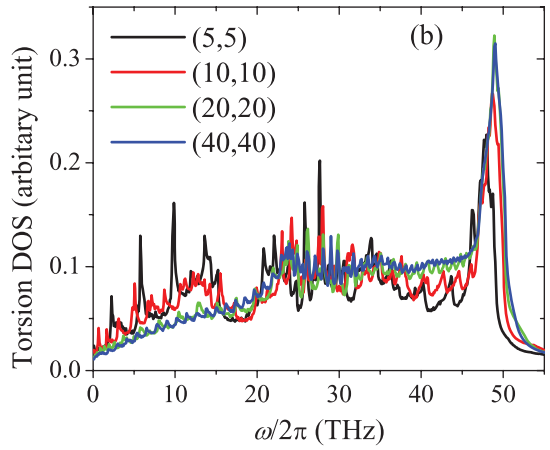

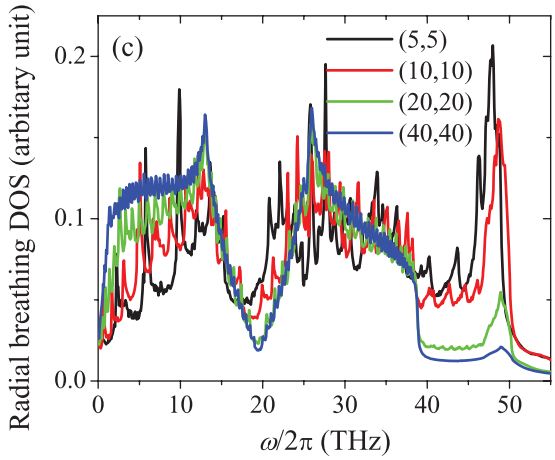

FIG. 8. The DOS of the longitudinal (a), twist (b), and the radial-breathing (c) modes in SWCNTs with different diameters (all 100 nm long) at $T = 300$ K. The radial breathing modes are more sensitive to the variation of SWCNT diameter at low and mediate frequency, comparing with the other two modes.

the diameter-dependence thermal conductivity in SWCNTs. Further analyses of Figure 8(c) indicate that smaller diameter tubes have relatively more high frequency (>40 THz) radial breathing modes, while larger diameter tubes have more low and moderate frequency range (<40 THz) modes in the radial direction. Again, we note that the DOS are computed on

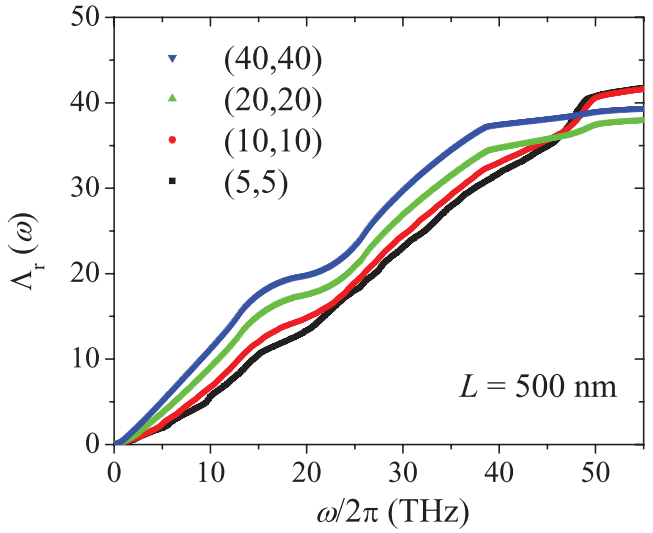

FIG. 9. Partial power spectrum $\Lambda_r(\omega)$ for armchair tubes of length 500 nm as a function of frequency, showing the increase of $\Lambda_r(\omega)$ with increasing diameter for frequencies lower than 40 THz.

a per-atom basis. Thus, the DOS curves for tubes of different diameters are comparable.

To further investigate the different frequency components in the total DOS, we consider the partial power spectrum defined below

$$\Lambda(\omega) = \sum_{\alpha} \Lambda_{\alpha}(\omega), \quad \Lambda_{\alpha}(\omega) = \int_0^{\omega} g(s)ds = \int_0^{\omega}\int_0^{1} E_{\alpha}(s,k_z)dk_z ds, \quad \alpha = z, r, \varphi. \tag{5}$$

Physically, $\Lambda(\omega)$ represents the power spectrum of all the phonon modes below frequency ω. Our simulation results show that the partial power spectrum of the longitudinal (LA) and twist (TA) modes is rather insensitive to the tube

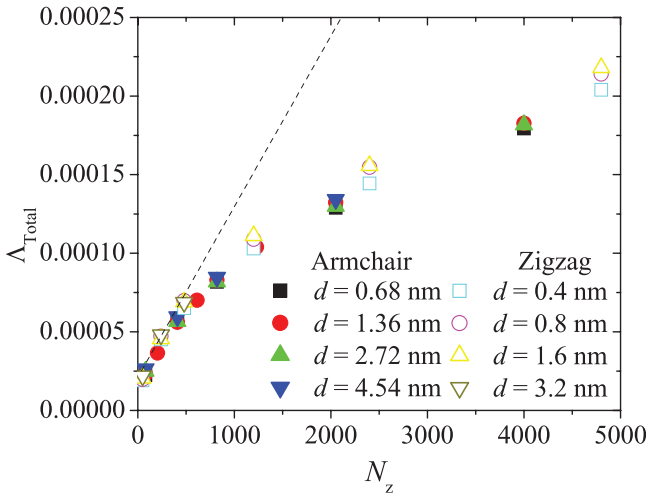

FIG. 10. The total power spectrum as a function of number of unit cells for various armchair and zigzag SWCNTs, showing all the data follow a universal behavior and a transition from linear to nonlinear dependence occurs at about 500 N_z, which corresponds to 200 nm for zigzag and 300 nm for armchair tubes, respectively. Note that the unit lengths of zigzag and armchair SWCNTs are different.

TABLE II. Comparison of the thermal conductivity of SWCNTs obtained from the present study and the available existing literature using various MD methods at room temperature.

Reference	κ (W/m K)	Length (nm)	Chirality	MD method	Potential	Boundary condition
Berber *et al.*[1]	6600	2.5	(10, 10)	HNEMD	Tersoff	PBC
Che *et al.*[28]	2980	40	(10, 10)	EMD	Brenner	PBC
Maruyama[12]	260 ~ 400	10-400	(10, 10)	NEMD	Brenner	PBC
Lukes *et al.*[13]	120 ~ 160	40	(10, 10)	NEMD	Brenner	PBC and non-PBC
Osman *et al.*[14]	1700	30	(10, 10)	NEMD	Tersoff–Brenner	PBC
Padgett and Brenner[15]	40-320	20-310	(10, 10)	NEMD	Brenner	PBC
Donadio and Galli[50]	7000	20	(10, 0)	EMD	Tersoff	PBC
Thomas *et al.*[16]	355	1000	(10, 10)	NEMD	REBO	Non-PBC
The present study	1580	2400	(10, 10)	NEMD	Optimized Tersoff	PBC

diameter (not shown). The partial power spectrum for the breathing (ZA) mode, $\Lambda_r(\omega)$, changes with tube diameter rather significantly, as shown in Figure 9. It is seen that up to about 40 THz, larger diameter tubes have more active radial breathing modes. Since low frequency modes (having finite group velocities, see Figure 4) are more effective in carrying heat, one may conclude that tubes with larger diameter have higher thermal conductivity because there are more active low frequency radial breathing modes. In addition, Figure 9 also shows that larger diameter tubes have less active high frequency radial breathing modes. However, these higher frequency modes do not contribute much to the thermal conductivity because of their near-zero group velocities, see Figure 4.

By including the entire frequency spectrum, one may obtain the total power spectrum $\Lambda_r(\infty)$. Plotted in Figure 10 is the total power spectrum $\Lambda(\infty) = \sum_\alpha \Lambda_\alpha(\infty)$ for all the SWCNTs studied in this paper. Interestingly, when $\Lambda(\infty)$ is plotted against N_z, the number of unit cells in the tube, the total power spectra for all the SWCNTs considered here, irrespective of their chirality, seem to fit into a single master curve, which agrees with the observation that the thermal conductivity of SWCNTs is not sensitive to chirality. Note that N_z is proportional to the tube length, albeit the proportional constant is different among tubes with different chiralities. Therefore, one may conclude from Figure 10 that the total power spectrum is independent of the tube diameter but increases monotonically with tube length.

As a footnote, we point out that the results shown in Figure 6 are consistent with a more recent study[30] for tubes with diameter greater than about 1.5 nm. For tubes with diameter less than about 1.5 nm, the phonon Boltzmann transport equation method predicts that the thermal conductivity starts to increase with decreasing tube diameter due to the violation of a selection rule in graphene arising from its reflection symmetry.[30] Such discrepancy between results of the phonon Boltzmann transport equation approach utilized in Ref. 30 and our MD results for extremely small tube diameters is being investigated. The results will be reported elsewhere.

Before closing, it is worthwhile to compare our results against previous work. First, our simulation results show that the thermal conductivity of a 2400 nm-long (10, 10) SWCNT is 1620 W/mK at room temperature. Experimentally measured value is 2000–3500 W/mK for a SWCNT of length 2600 nm and diameter 1.7 nm (corresponding to (12, 12) studied here) at room temperature.[16] Second, since the non-equilibrium MD method is used in our studies, it is fair to compare with the results obtained by the same method. Maruyama *et al.*[48] obtained 380 W/mK for a (10, 10) SWCNT at length of 200 nm with a simplified Brenner potential. Our result of (10, 10) tube with the same length and diameter is 860 W/mK. Thomas *et al.*[16] predicted ~380 W/mK for a (10, 10) tube of length 800 nm using the Reactive Empirical Bond Order (REBO) potential. Our results of (10, 10) tube with the same length and diameter is 1350 W/mK. The comparison of the thermal conductivity of SWCNTs obtained from the present study and the available existing literature using various MD methods is shown in Table II. We are also aware that recent work on graphene nanoribbon showed that the thermal conductivity of graphene nanoribbon increases with width and become independent of width when exceeding 500 nm, reaching the limit of an infinite graphene sheet.[49]

IV. SUMMARY AND CONCLUSIONS

In summary, non-equilibrium MD simulations are carried out in this paper to study the thermal transport behavior in micrometer-long SWCNTs comparable to experimental samples. Particular attention is given to the effects of tube length and diameter on the thermal conductivity. We found that the transition length from predominately ballistic to ballistic-diffusive transport is about $l_0 = 200$ nm for zigzag and $l_0 = 300$ nm armchair SWCNTs regardless of their diameters. In other words, in tubes that are less l_0, thermal transport is predominately ballistic. Thermal resistance in this ballistic regime is caused predominately by phonon scattering at the boundary, and the thermal conductivity scales up linearly with the tube length. In tubes that are longer than l_0, thermal transport is both ballistic and diffusive. In this ballistic-diffusive regime, both phonon boundary scattering and phonon-phonon scattering contribute to the thermal resistance, but the contribution from boundary scattering decreases as the tube length increases. Thus, thermal conductivity increases as a power-law function $\kappa \sim L^\alpha$.

Our results on the effects of tube diameter show that, in both armchair and zigzag SWCNTs, thermal conductivity increases exponentially with increasing tube diameter and eventually approaches that of graphene. We conclude that

such increase is attributed to the presence of more low and moderate frequency radial breathing modes in larger diameter tubes.

Finally, by combining the results on both length and diameter dependence, we found that the thermal conductivity of SWCNT can be described by $\kappa(L,d) \approx \kappa_g(L)(1-e^{-0.185d/a_0})$, where L is the tube length, d is the diameter, $a_0 = 2.46$ Å is the graphene lattice constant, and $\kappa_g(L) \propto L^{\alpha}$ is the thermal conductivity of graphene of length L. In the above, $\alpha = 1$ for $L < l_0$, and $\alpha \sim 0.21$ for $L > l_0$, where $l_0 = 200$ nm for zigzag and $l_0 = 300$ nm armchair SWCNTs are the effective phonon mean free paths for zigzag and armchair tubes, respectively.

ACKNOWLEDGMENTS

Computations were performed on the QUEST high performance computing cluster at Northwestern University. The work is supported in part by DARPA through Contract N66001-09-C-2012. The views expressed are those of the authors and do not reflect the official policy or position of the Department of Defense or the U.S. Government.

[1]S. Berber, Y.-K. Kwon, and D. Tomanek, Phys. Rev. Lett. **84**(20), 4613–4616 (2000).
[2]A. A. Balandin, Nature Mater. **10**(8), 569–581 (2011).
[3]A. A. Balandin, S. Ghosh, W. Z. Bao, I. Calizo, D. Teweldebrhan, F. Miao, and C. N. Lau, Nano Lett. **8**(3), 902–907 (2008).
[4]A. Cao, J. Appl. Phys. **111**, 083528 (2012).
[5]D. L. Nika, E. P. Pokatilov, A. S. Askerov, and A. A. Balandin, Phys. Rev. B **79**(15), 155413 (2009).
[6]D. L. Nika and A. A. Balandin, J. Phys.: Condens. Matter. **24**, 233203 (2012).
[7]S. S. Chen, Q. Z. Wu, C. Mishra, J. Y. Kang, H. J. Zhang, K. J. Cho, W. W. Cai, A. A. Balandin and R. S. Ruoff, Nature Mater. **11**(3), 203–207 (2012).
[8]Z. Aksamija and I. Knezevic, Appl. Phys. Lett. **98**(14), 141919 (2011).
[9]R. Saito, M. Fujita, G. Dresselhaus, and M. S. Dresselhaus, Phys. Rev. B **46**(3), 1804–1811 (1992).
[10]W. Yi, L. Lu, D. L. Zhang, Z. W. Pan, and S. S. Xie, Phys. Rev. B **59**(14), R9015–R9018 (1999).
[11]Z. H. Yao, J. S. Wang, B. W. Li, and G. R. Liu, Phys. Rev. B **71**(8), 085417 (2005).
[12]S. Maruyama, Microscale Thermophys. Eng. **7**(1), 41–50 (2003).
[13]J. R. Lukes and H. Zhong, J. Heat Transfer **129**(6), 705–716 (2007).
[14]M. A. Osman and D. Srivastava, Nanotechnology **12**(1), 21–24 (2001).
[15]C. W. Padgett and D. W. Brenner, Nano Lett. **4**(6), 1051–1053 (2004).
[16]J. A. Thomas, R. M. Iutzi, and A. J. H. McGaughey, Phys. Rev. B **81**, 045413 (2010).
[17]P. Kim, L. Shi, A. Majumdar, and P. L. McEuen, Phys. Rev. Lett. **87**(21), 215502 (2001).
[18]M. Fujii, Z. Xing, X. Huaqing, H. Ago, K. Takahashi, T. Ikuta, H. Abe, and T. Shimizu, Phys. Rev. Lett. **95**(6), 065502 (2005).
[19]C. Yu, L. Shi, Z. Yao, D. Li, and A. Majumdar, Nano Lett. **5**(9), 1842–1846 (2005).
[20]E. Pop, D. Mann, J. Cao, Q. Wang, K. Goodson, and H. J. Dai, Phys. Rev. Lett. **95**(15), 155505 (2005).
[21]T.-Y. Choi, D. Poulikakos, J. Tharian, and U. Sennhauser, Nano Lett. **6**(8), 1589–1593 (2006).
[22]X. W. Wang, Z. R. Zhong, and J. Xu, J. Appl. Phys. **97**(6), 064302 (2005).
[23]E. Pop, D. Mann, Q. Wang, K. Goodson, and H. Dai, Nano Lett. **6**(1), 96–100 (2006).
[24]J. Shiomi and S. Maruyama, Phys. Rev. B **73**(20), 205420 (2006).
[25]N. Mingo and D. A. Broido, Nano Lett. **5**(7), 1221–1225 (2005).
[26]Y. F. Gu and Y. F. Chen, Phys. Rev. B **76**(13), 134110 (2007).
[27]L. Lindsay, D. A. Broido, and N. Mingo, Phys. Rev. B **80**(12), 125407 (2009).
[28]J. W. Che, T. Cagin, and W. A. Goddard, Nanotechnology **11**(2), 65–69 (2000).
[29]N. Mingo and D. A. Broido, Phys. Rev. Lett. **95**(9), 4 (2005).
[30]L. Lindsay, D. A. Broido, and N. Mingo, Phys. Rev. B **82**(16), 161402 (2010).
[31]L. Lindsay and D. A. Broido, Phys. Rev. B **81**(20), 205441 (2010).
[32]A. Cao and J. Qu, J. Appl. Phys. **111**, 053529 (2012).
[33]T. Yamamoto, S. Watanabe, and K. Watanabe, Phys. Rev. Lett. **92**(7), 075502 (2004).
[34]J. Hone, M. Whitney, C. Piskoti, and A. Zettl, Phys. Rev. B **59**(4), R2514–R2516 (1999).
[35]J. A. Wang and J. S. Wang, Appl. Phys. Lett. **88**(11), 111909 (2006).
[36]P. Jund and R. Jullien, Phys. Rev. B **59**(21), 13707–13711 (1999).
[37]S. Plimpton, J. Comput. Phys. **117**(1), 1–19 (1995).
[38]J. Tersoff, Phys. Rev. B **38**(14), 9902–9905 (1988).
[39]D. W. Brenner, Phys. Rev. B **42**(15), 9458 (1990).
[40]M. Mohr, J. Maultzsch, E. Dobardzic, S. Reich, I. Milosevic, M. Damnjanovic, A. Bosak, M. Krisch, and C. Thomsen, Phys. Rev. B **76**(3), 035439 (2007).
[41]J. Maultzsch, S. Reich, C. Thomsen, H. Requardt, and P. Ordejon, Phys. Rev. Lett. **92**(7), 075501 (2004).
[42]V. N. Popov and P. Lambin, Phys. Rev. B **73**(8), 085407 (2006).
[43]M. S. Dresselhaus and P. C. Eklund, Adv. Phys. **49**(6), 705–814 (2000).
[44]R. Saito, G. Dresselhaus and M. S. Dresselhaus, *Properties of Carbon Nanotubes* (Imperial College Press, London, 1998).
[45]L. Vanhove, Phys. Rev. **89**(6), 1189–1193 (1953).
[46]J. S. Heo and M. Bockrath, Nano Lett. **5**(5), 853–857 (2005).
[47]D. Sanchez-Portal, E. Artacho, J. M. Soler, A. Rubio, and P. Ordejon, Phys. Rev. B **59**(19), 12678–12688 (1999).
[48]S. Maruyama, Physica B **323**(1–4), 193–195 (2002).
[49]E. Munoz, J. X. Lu, and B. I. Yakobson, Nano Lett. **10**(5), 1652–1656 (2010).
[50]D. Donadio and G. Galli, Nano Lett. **10**(3), 847–851 (2010).